Microstructures and mechanical properties of a L1$_2$-structured precipitation strengthened Co-based superalloy

Zhouqing Zhang [a], Qingqing Ding [a,***], Yilun Gong [b], Xiao Wei [a], Ze Zhang [a,c,**], Hongbin Bei [a,*]

[a] School of Materials Science and Engineering, Zhejiang University, Hangzhou 310027, China
[b] Max-Planck-Institut für Eisenforschung, Max-Planck-Straße 1, Düsseldorf 40237, Germany
[c] State Key Laboratory of Silicon Materials, Zhejiang University, Hangzhou 310027, China

ARTICLE INFO

ABSTRACT

A L1$_2$-structured precipitation (γ') strengthened Co-based superalloy is identified based on thermodynamic calculation and experimental validation. An alloy with composition of Co9Al5Mo30Ni2Ta10Cr is fabricated to explore the relationships among processing, microstructures and mechanical properties. Typical γ/γ' two-phase microstructures have been obtained after heat treatments, where the spherical γ' phase with diameter of ~100 nm is uniformly distributed in the face centered cubic (FCC) matrix. The L1$_2$ structured γ'-(Ni, Co)$_3$(Al, Ta) phase can be stabilized, which coherently precipitates in the FCC matrix (γ) during aging treatment. The alloy exhibits promising strength with comparison to traditional Co-based superalloys at a temperature range from room temperature (RT) to 1000 °C. The predominant deformation mechanism transits from shearing of dislocation pairs to dislocations bypassing γ' phase when deformation temperature increases from RT to 1000 °C.

1. Introduction

Both Ni- and Co-based superalloys occupy important positions in the history of superalloys and are widely applied in numerous fields as structural materials [1−3]. As the most commercially successful superalloys, Ni-based superalloys have superior high temperature strength, which results from a stable two-phase microstructure containing L1$_2$- γ' coherent precipitates (Ni$_3$Al) uniformly distributed in a face-centered cubic (FCC) γ-matrix [2,4]. Co-based superalloys generally have better oxidation and hot corrosion resistance [5−7]. The melting point of Co is 1495 °C, 40 °C higher than that of Ni (1455 °C), which could be regarded as a potential capability for improving service temperature of the alloy. However, the strength of Co-based superalloys is commonly achieved by solid solution or carbide strengthening [8−10], which results in the relatively lower strength than that of Ni-based superalloys and thus limits industry application of Co-based superalloys.

Over the last decades, alloy design and development through precipitation strengthening in Co-based superalloys continuously remain a research frontier in the high temperature material field [3,8—11]. The main challenge is that, unlike Ni₃Al with L1₂ ordered structure, the phase Co₃Al is metastable in Co—Al system and it tends to form B2—CoAl phase [12], which cannot provide effective strengthening for the alloy and the intermetallic CoAl phase itself is brittle below ductile to brittle transition temperature (DBTT). Until 2006, Sato et al. [11] report that W addition can stabilize γ′-Co₃(Al, W) phase with L1₂ ordered structure in a ternary alloy Co-9.2Al—9W, which provides a new possibility to develop Co-based superalloys with precipitation strengthening, just similar to the Ni-based single crystal superalloys [4,13]. From then, various efforts have been exerted to explore effects of alloying addition on the microstructures, mechanical
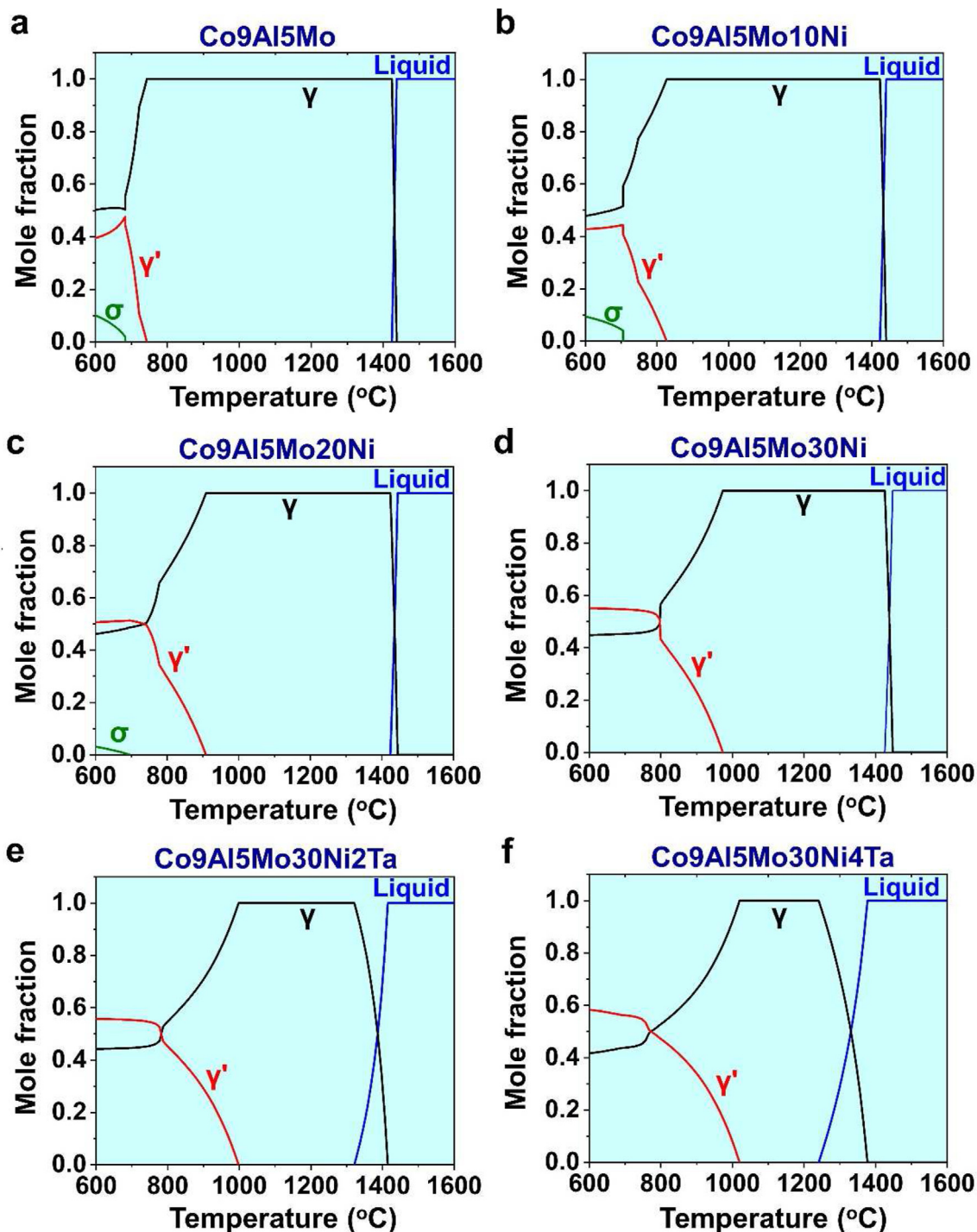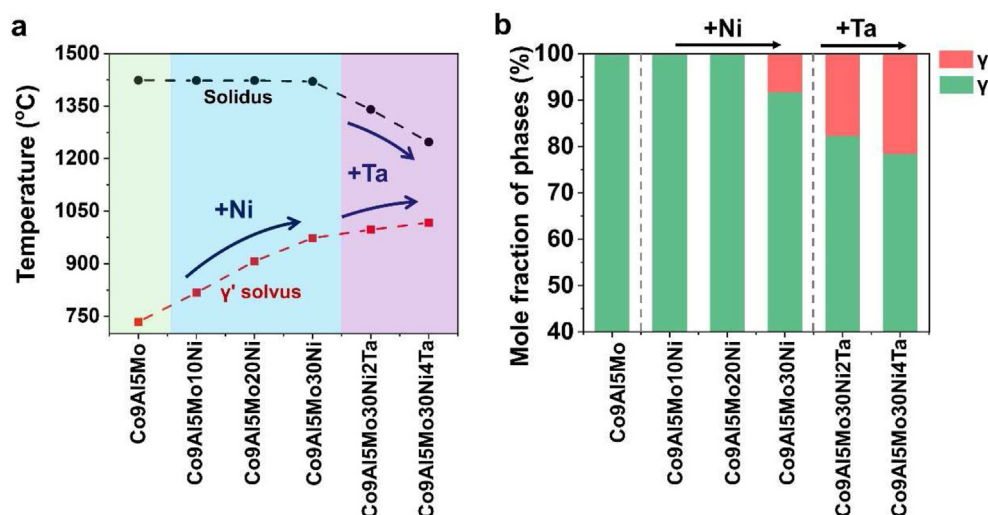

Fig. 1 — The temperature dependence of phase fraction under thermodynamic equilibrium for (a) Co9Al5Mo,
(b) Co9Al5Mo10Ni, (c) Co9Al5Mo20Ni, (d) Co9Al5Mo30Ni, (e) Co9Al5Mo30Ni2Ta and (f) Co9Al5Mo30Ni4Ta alloys.

Fig. 2 – (a) The calculated γ' solvus, solidus temperatures and (b) mole fraction of the phases at 950 °C, as a function of additions of Ni and Ta, based on Co9Al5Mo, Co9Al5Mo10Ni, Co9Al5Mo20Ni, Co9Al5Mo30Ni, Co9Al5Mo30Ni2Ta and Co9Al5Mo30Ni4Ta.

properties and phase stability with the aim to develop precipitation strengthened Co-based superalloys. Generally, Mo can provide solid solution strengthening for the matrix [14], but high Mo concentration would induce other harmful phases, such as topological close packed (TCP) phases [15–19]. Ta and Ni are two of the most important elements to stabilize γ' phase and increase γ' phase solvus temperature [20–22]. Additionally, Cr plays a crucial role in oxidation and corrosion resistance [23,24]. Similar to Mo, high concentration of Cr can facilitate the formation of TCP phases. For example, Chen and Yan et al. reported that Cr addition above ~10 at.% facilitates formation of μ and β phases, and therefore decrease the creep properties of Co–Al–W and Co–Ni–Al–W alloys [25–28].

Briefly, although several L1$_2$-structured γ' precipitation strengthened Co-based superalloys have been successfully developed, such as Co–Al–W [11,15–19], Co–Ni–Al–Ta/Nb [20,22], Co–Ni–Cr–Al–Mo–Ta/Nb [20,29], Co–Al–V/Ta [30–32], etc., multicomponent precipitation strengthened Co-based superalloys are still under development and have restricted their applications, with comparison to Ni-based superalloys. Here, with the aid of thermodynamic calculation, Co9Al5Mo30Ni2Ta is selected as the base alloy for further experimental validation. Alloying elements Ni and Ta are added to stabilize the L1$_2$-structured γ' phase and Mo is added to strengthen the matrix. For further balancing oxidation resistance and ductility of the alloy, Cr and B are added and investigated experimentally. A L1$_2$-structured precipitation strengthened Co-based superalloy is successfully fabricated. Moreover, to reveal the relationship among the processing, microstructures and mechanical properties, the microstructures during different processing steps, before and after mechanical tests, are investigated by using scanning electron microscopy (SEM) and scanning/transmission electron microscopy (S/TEM) and the temperature effects on the deformation mechanism are briefly discussed.

2. Thermodynamic calculation

In Co-based solid solution superalloys, Mo is usually added as an important strengthening element [14]. Al is the essential element for developing precipitation strengthened Co–Al system superalloys. When the CALPHAD method is adopted to screen the alloy composition by using ThermoCalc software with a TCHEA6 database, addition of γ' stabilizers, such as Ni and Ta, are considered with Co–Al–Mo ternary system as the start point. In order to ensure the phase/microstructure stability of screened alloy at high temperature, two principles are considered: (1) the melting point of the alloy, solvus temperature and mole fraction of γ' phase should be as high as possible, (2) it is better that no TCP phases appear.

Fig. 1 shows some examples of thermodynamic calculation, which are the temperature dependence of phase fraction under thermodynamic equilibrium of several compositions. In Co9Al5Mo and Co9Al5Mo10/20Ni (Fig. 1a–c), the equilibrium phases include liquid phase, γ, γ' and σ (TCP) phases. In Co9Al5Mo30Ni and Co9Al5Mo30Ni2Ta/4Ta (Fig. 1d–f), there are only three phases, including liquid phase, γ and γ' phases, and the σ phase disappears. Moreover, with increasing Ni concentration and the addition of Ta, it seems that the solvus temperature and mole fraction of γ' phase increase.

Fig. 2 further summarizes the calculated γ' solvus, solidus temperature and mole fraction of phases at 950 °C, as a function of additions of Ni and Ta. The γ' phase solvus temperature is calculated to be as low as 734 °C in ternary Co9Al5Mo alloy. A large single-phase FCC region exists above 734 °C up to the solidus temperature (1424 °C). With Ni addition increasing from 10 to 30 at.%, the γ' solvus temperature increases by 156 °C without decreasing solidus temperature (Fig. 2a). And the mole fraction of γ' phase increases to ~10% at 950 °C in Co9Al5Mo30Ni, while there's no γ' phase in

Table 1 − Nominal and measured (EDS quantification) compositions (at.%) of Co9Al5Mo30Ni2Ta15CrB (Co001) and Co9Al5Mo30Ni2Ta10CrB (Co002) alloys.

Elements		Co	Ni	Al	Cr	Mo	Ta	B
Co001 alloy	Nominal	Bal.	30	9	15	5	2	0.03
	Measured	Bal.	30.1	8.5	15.2	5.3	2.0	~
Co002 alloy	Nominal	Bal.	30	9	10	5	2	0.03
	Measured	Bal.	30.2	8.4	10.2	5.4	2.1	~

Co9Al5Mo alloys with 0Ni, 10Ni and 20Ni at 950 °C (Fig. 2b). Furthermore, with 2 at.% Ta addition in Co9Al5Mo30Ni2Ta alloy, the calculated γ′ solvus temperature increases to higher than 1000 °C and the mole fraction of γ′ phase at 950 °C reaches up to ~20%. However, further increasing Ta addition to 4 at.% does not affect the γ′ solvus temperature significantly but rapidly decreases the solidus temperature by ~90 °C (Fig. 2a). Therefore, Co9Al5Mo30Ni2Ta is selected as the base alloy for further experimental validation.

In addition, Cr is added to improve resistance to oxidation, which is essential for high temperature applications of Co-based superalloys [4,23,24]. However, high concentration Cr can facilitate formation of TCP phases, and thus, the Cr addition is controlled to be as high as possible but lower than the critical concentration for TCP phases [25−28]. It is found that TCP phases can be avoided when Cr concentration is lower than 10 at.% in Co−Al−W and Co−Ni−Al−W alloys [25−28]. Therefore, 10 and 15 at.% Cr additions are investigated experimentally. Moreover, because B, as a trace element, is normally added in precipitation strengthened Ni-based superalloys to strengthen grain boundary [2,8,33], 0.03 at.% B is also added. Collectively, two alloy compositions (as shown in Table 1) are subsequently fabricated and thermal mechanical processed and their microstructures are carefully experimentally investigated.

3. Material and methods

3.1. Material preparation

The material is prepared from the constituent elements Co, Ni, Al, Cr, Mo, Ta and B (higher than 99.9% purity), through arc melting in an Ar atmosphere in a water-chilled copper hearth. The alloy ingot is flipped and re-melted more than five times to ensure chemical homogeneity, and then drop-cast into a water-chilled Cu mold with a dimension of $12.5 \times 12.5 \times 120$ mm^3. The total weight is 200 g and the total weight loss of the ingot is less than 0.2%. Therefore, the as-cast alloy is assumed to have the desired composition, which is also confirmed by energy dispersive spectroscopy (EDS) quantification shown in Table 1. The element B is not included in EDS quantification because EDS analysis of light elements with atomic number Z less than 11 is not reliable.

3.2. Differential scanning calorimetry (DSC) and heat treatment

Phase transformation temperatures of the alloys are investigated by a Netzsch DSC 404 (NETZSCH-GmbH, Germany) instrument. The complete DSC cycle is heating from RT to 1470 °C and then cooling to 200 °C at a rate of 20 °C/min. All tests are conducted in a purged high-purity argon with flow rate of 20 mL/min. Melting temperatures and phase transformation temperatures are determined from heating curves with Netzsch Proteus Thermal Analysis software (NETZSCH-GmbH, Germany).

The heat treatment experiments are carried out in a vacuum/Ar protected tube furnace, in which the heating rate and holding temperature can be program controlled. Before heating, the tube furnace is evacuated to a vacuum of <1 Pa and then followed by refilling with high purity argon.

3.3. Tensile testing

The 0.2% offset yield strength (YS) and elongation to fracture (EF) are evaluated by tensile testing at a temperature range from RT to 1000 °C. The recrystallized plate is cut into dog-bone-shape specimens with gauge sections about $1.8 \times 1.5 \times 9.5$ mm^3 by electro-discharge machining (EDM). The surfaces of the gauge section are carefully ground with 600 grit SiC paper to eliminate oxide layers and microcracks that may be introduced during EDM. Tensile tests are conducted on a screw-driven mechanical testing machine equipped with an induction heater at laboratory atmosphere.
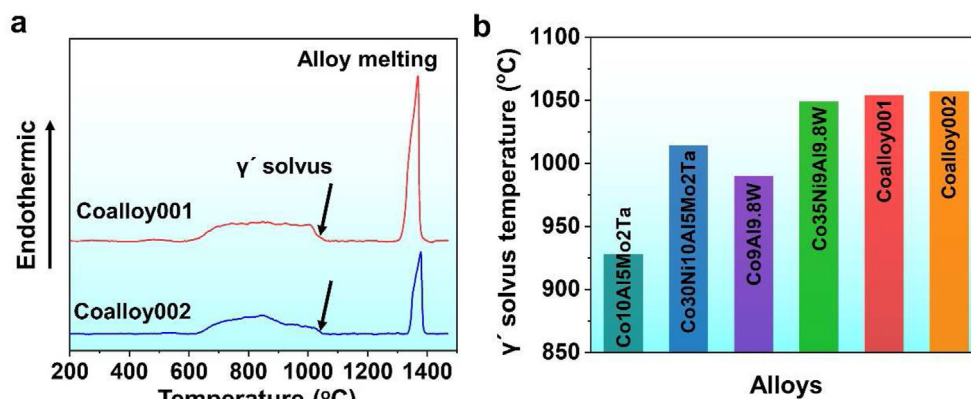
Fig. 3 − (a) DSC heating curves of Co001 and Co002 alloys. (b) The measured γ′ solvus temperature of Co001 and Co002 alloys, which are higher than Co10Al5Mo2Ta, Co30Ni10Al5Mo2Ta, Co9Al9.8W and Co35Ni9Al9.8W precipitation strengthened Co-based superalloys [4,20,39].

A thermocouple is in direct contact with the sample gauge section to monitor testing temperature within ±3 K of the set temperature for elevated temperature tensile testing. In addition, tensile samples are heated to testing temperature by the induction heater and hold at least 15 min before applying load. All the samples are tested at a constant cross head displacement rate of 0.57 mm/min, which corresponds to an engineering strain rate of 10^{-3} s^{-1}. The length (marked by two Vickers hardness indentation impression in the gauge section) before and after fracture are measured to calculate the EF. The YS is calculated using 0.2% offset method.

3.4. Microstructure characterization

To observe the microstructure, samples with a thickness of 1—2 mm are cut by EDM and ground down to 1200 grit SiC paper, followed by mechanical polishing. Some polished samples are electrochemical polished in phosphoric acid to better reveal the microstructure. The SEM images are all captured in a FEI quanta 650 SEM using an accelerating voltage of 15 kV and a 10 mm working distance, equipped with a secondary electron (SE) detector, a back scattered electron (BSE) detector, and an Oxford EDS detector.

Thin foils with diameter ~3 mm punched from the heat treated and tensile deformed specimens are ground to a thickness of ~50 μm and then twin-jet electropolished in an alcoholic solution containing 5 vol% perchloric acid at −30 °C. TEM imaging and quantitative composition analysis of γ and γ′ phases are carried out on a Tecnai G^2 F20 TEM and a spherical aberration corrected FEI Titan G^2 TEM, which are operated at 200 kV. High angle annular dark field (HAADF) and ADF STEM images were all captured on the latter TEM.

3.5. Measurement of the stacking fault energy (SFE)

The SFE (γ_{sf}) of the matrix can be estimated by the following equation [34—38],

$$\gamma_{sf} = \frac{Gb_p^2}{8\pi d}\left(\frac{2-\nu}{1-\nu}\right)\left(1 - \frac{2\nu\cos2\theta}{2-\nu}\right) \tag{3-1}$$

where G is shear modulus, b_p is the length of the Burgers vector of the partial dislocation, ν is Poisson's ratio, d is the width of dislocation core and θ is the angle between the dislocation line and the burgers vector of the full dislocation.

4. Results and discussion

4.1. γ′ solvus temperature

Fig. 3a shows DSC heating curves of Co001 and Co002 alloys, where the first endothermic peak corresponds to γ′ solvus temperature (pointed by the black arrows) and the second is the melting peak of the alloy. Melting temperatures of Co001 and Co002 alloys are determined to be 1303 and 1324 °C, respectively. And γ′ solvus temperatures of Co001 and Co002 alloys are determined to be 1054 and 1059 °C respectively, which are both around 60 °C higher than the calculated results. Fig. 3b shows that γ′ solvus temperatures of Co001 and Co002 alloys are slightly higher than Co35Ni9Al9.8W and Co30Ni10Al5Mo2Ta alloys, and much higher than Co10Al5-Mo2Ta and Co9Al9.8W alloys [4,20,39], which indicates that the thermodynamic calculation is effective to guide alloy design. According to DSC results, as-cast ingots are homogenized at 1250 °C for 4 h followed by water cooling (WC). The homogenized bars are cold rolled along longitudinal ingot direction to a total thickness reduction of ~80%. The cold
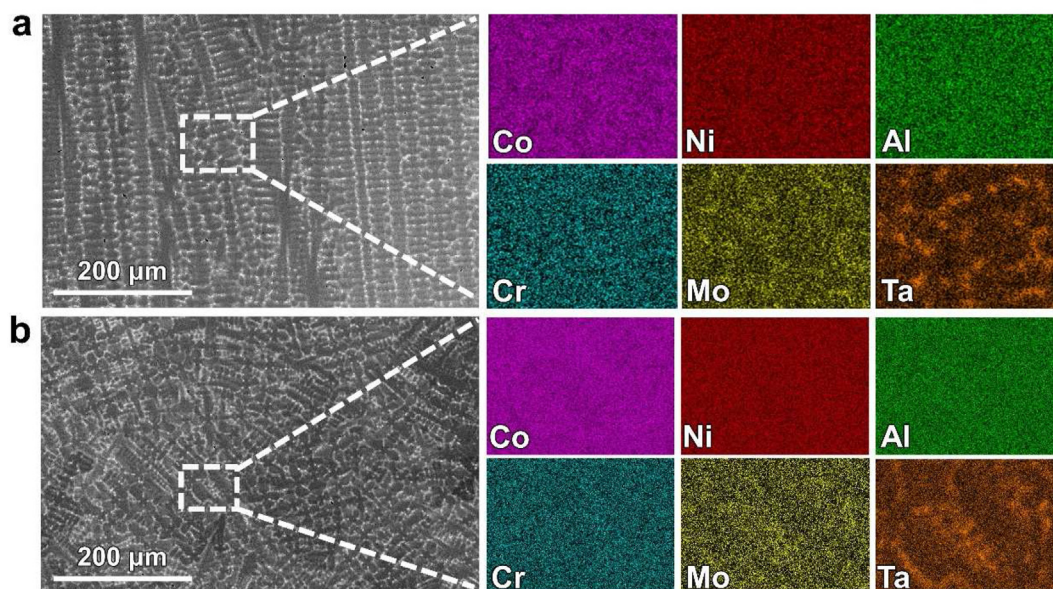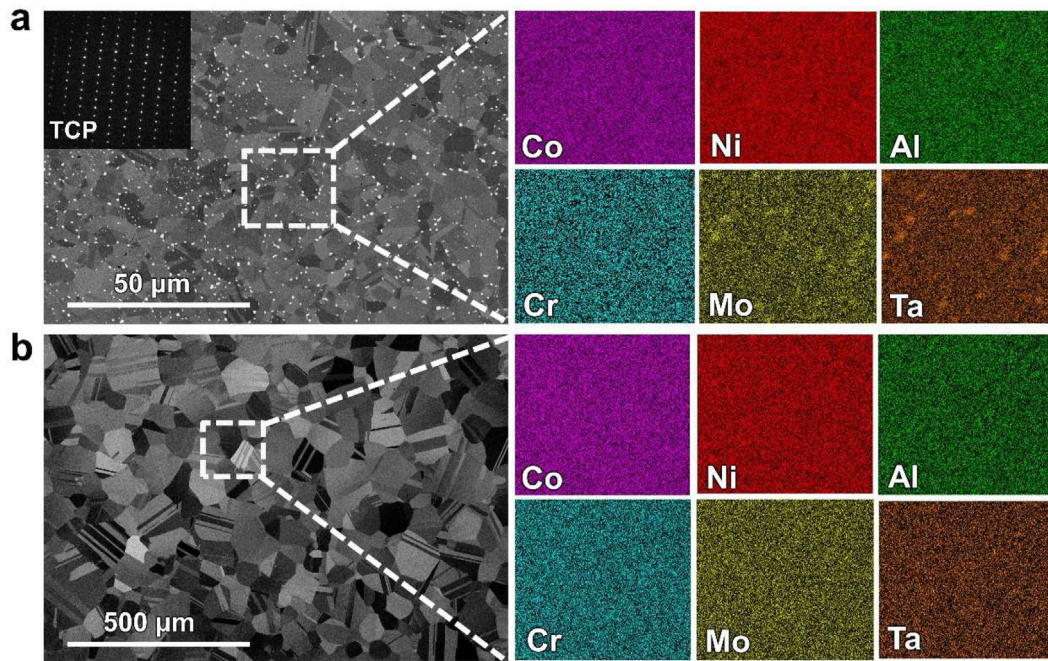

Fig. 4 — BSE images and corresponding EDS maps of the area indicated by rectangle of as cast (a) Co001 and (b) Co002 alloys, showing that both alloys exhibit typical dendritic structure and Ta and Mo are segregated in interdendritic regions.

Fig. 5 − BSE images and corresponding EDS maps of (a) Co001 and (b) Co002 alloys after recrystallization. Both Co001 and Co002 alloys show equiaxed grains, but with different grain sizes, which is ~10 μm for Co001 (a) and ~70 μm for Co002 (b). Notably that there are precipitations with bright contrast distributed in the Co001 alloy. SAED pattern (the inset in [a]) and EDS maps demonstrate that these precipitations are TCP phase rich in Ta and Mo. But no TCP phase is observed and all elements are uniformly distributed in Co002 alloy.

rolled plates are then recrystallized at 1050 °C for 1 h (WC) and finally aged at 950 °C for 4 h followed by air cooling (AC).

4.2. Microstructural evolution and phase analysis

Both Co001 and Co002 alloys exhibit typical dendritic structures, as shown in Fig. 4a & b, which are normally found in as-cast alloys due to constitutional supercooling during solidification process [40]. Under BSE imaging mode, dendrites are darker than interdendritic regions, indicating that heavy elements segregate in interdendrites, which are confirmed to be Ta and Mo by EDS analysis (Fig. 4a & b).

After homogenization, cold rolling and recrystallization, both Co001 and Co002 alloys exhibit equiaxed grains, but the average grain sizes are different, which is ~10 μm for Co001 alloy (Fig. 5a) and ~70 μm for Co002 alloy (Fig. 5b). The small grain size of Co001 alloy might be attributed to the precipitations with bright contrast, which are uniformly distributed in the alloy. Selected area diffraction pattern (SADP) and EDS maps (Fig. 5a) demonstrate that these precipitates are TCP phase rich in Ta and Mo. EDS quantification reveals that composition of the TCP phase is Co-19.0Ni-3.2Al-15.5Cr-15.3Mo-8.0Ta (at.%), as shown in Table 2, thus, the Co001

alloy with 15 at.% Cr is easy to form TCP phase. And the microstructural and elemental inhomogeneity have been eliminated in the Co002 alloy, where all elements are uniformly distributed in the alloy after recrystallization, indicated by EDS maps in Fig. 5b. Generally, TCP phases are brittle and consume strengthening elements, therefore damage mechanical properties of the alloy [4]. Therefore, the Cr addition for the Co−Al−Mo−Ni−Ta−Cr system alloy should be lower than 15 at.% and Co001 alloy is not considered for further investigation.

Fig. 6 shows microstructure of the Co002 alloy after recrystallization and aging, clearly indicating that a L1$_2$-structured γ′ precipitation strengthened Co-based superalloy is obtained. Fig. 6a & b are SE images of the recrystallized and aged samples, respectively. There are small amounts of precipitates with diameter about 30~50 nm after recrystallization (Fig. 6a). After aging, large amounts of spherical precipitates with diameter of ~100 nm uniformly distribute in the matrix (Fig. 6b), indicating that these spherical precipitates are mainly precipitated during aging, which is similar to the process of precipitation strengthened Ni-based superalloys [4,41]. In addition, the area fraction of precipitations is measured to be about 55%. EDS results (Fig. 6c) reveal that

Table 2 − Compositions (at.%) of the TCP phase and matrix in Co001 alloy.						
Elements	Co	Ni	Al	Cr	Mo	Ta
TCP phase	39.0 ± 0.3	19.0 ± 0.2	3.2 ± 0.5	15.5 ± 0.1	15.3 ± 0.4	8.0 ± 0.3
Matrix	38.4 ± 0.2	30.5 ± 0.3	8.3 ± 0.5	15.6 ± 0.1	5.2 ± 0.2	2.0 ± 0.1
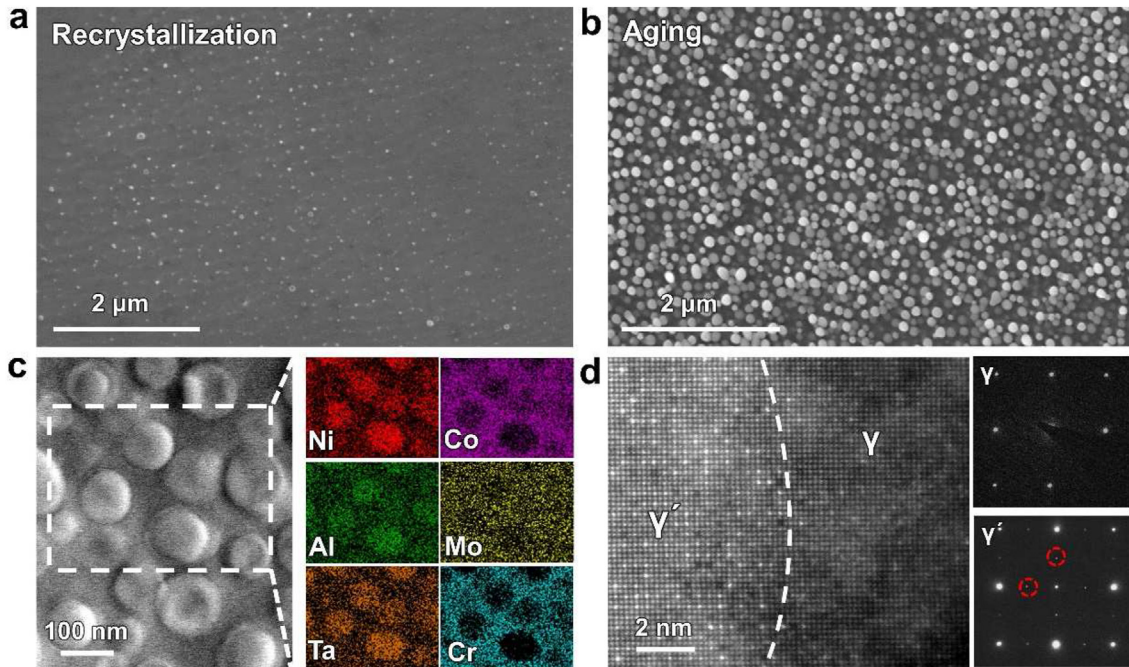
Fig. 6 — Microstructures of the Co002 alloy. (a, b) SE images of the recrystallized (a) and aged (b) alloys, respectively. A large number of spherical precipitates with ~55% area fraction are uniformly distributed in the matrix. (c) STEM image and corresponding EDS maps of the aged alloy show that the spherical precipitate is rich in Ni, Al and Ta, while the matrix is rich in Co, Mo and Cr. (d) Atomic resolution HAADF-STEM image indicates that the matrix and precipitate is coherent, with viewing direction along [001] direction. The interface between the two phases is indicated by dash line. Insets in (d) are SADPs of the two phases in aged alloy along [001] zone axes, indicating that the matrix is FCC structured (γ phase) and the precipitate is L1$_2$ ordered structured (γ' phase). Some superlattices of γ' phase are indicated by dash circles.

these spherical precipitates are rich in Ni, Al and Ta, while the matrix is rich in Co, Cr and Mo. Quantified EDS analysis of the two phases are shown in Table 3. It is found that average composition of precipitates is 31.2Co-41.0Ni-15.1Al-3.3Cr-3.7Mo-5.7Ta, and that of the matrix is 46.2Co-27.4Ni-6.3Al-12.7Cr-6.2Mo-1.2Ta (at.%). Fig. 6d is the atomic resolution HAADF-STEM image, demonstrating that the precipitate is coherent with the matrix. To reveal the crystal structures of the matrix and these spherical precipitates, SADPs of the two phases have been captured with viewing direction along [001], as shown as insets of Fig. 6d. The matrix is FCC structure, which is often called γ phase. Superlattices of precipitates (some are indicated by red dash circles) indicate that precipitates are L1$_2$ structured, which is the so-called γ' phase. Combined with the EDS analysis and TEM characterization, these spherical precipitates are determined to be intermetallic (Ni, Co)$_3$(Al, Ta) with L1$_2$-ordered structure.

Generally, absolute value of the lattice mismatch (/δ/) between matrix and precipitate determines morphology of the precipitate [42—46]. The lattice mismatch between γ and γ' phases (δ) can be determined by $\delta = 2(a_{\gamma'}-a_{\gamma})/(a_{\gamma'}+a_{\gamma})$, where a_{γ}

and $a_{\gamma'}$ are lattice parameters of γ and γ' phases, respectively. If /δ/ is lower than 0.3%, precipitates are likely to be spherical, while with the /δ/ increases, precipitates become cubic [42,47—49]. From the SADPs, lattice parameters of γ and γ' phases in Co002 alloy are determined to be 0.3580 and 0.3587 nm, respectively. Therefore, δ is only about +0.2%, which is consistent with the spherical morphology of γ' precipitates.

4.3. Mechanical properties and fracture analysis

Tensile properties of recrystallized and aged Co002 alloys are measured over a temperature range from RT to 1000 °C and the results are shown in Fig. 7. Engineering stress-strain curves (Fig. 7a and b) indicate that, at temperature below 600 °C, two alloys experience continuous work hardening before failure. At temperatures above 600 °C, alloys fracture after yielding with limited plastic deformation. Due to the relatively high area fraction of γ' phase, YS of the aged alloy is higher than that of the recrystallized alloy in the entire test temperature range. The YS of the aged alloy is higher than

| Table 3 — Compositions (at.%) of the γ-matrix and γ' phase in Co002 alloy measured by EDS.						
Elements	Co	Ni	Al	Cr	Mo	Ta
γ'	31.2 ± 0.6	41.0 ± 0.1	15.1 ± 0.8	3.3 ± 0.1	3.7 ± 0.3	5.7 ± 0.3
γ	46.2 ± 0.4	27.4 ± 0.3	6.3 ± 0.9	12.7 ± 0.2	6.2 ± 0.4	1.2 ± 0.2
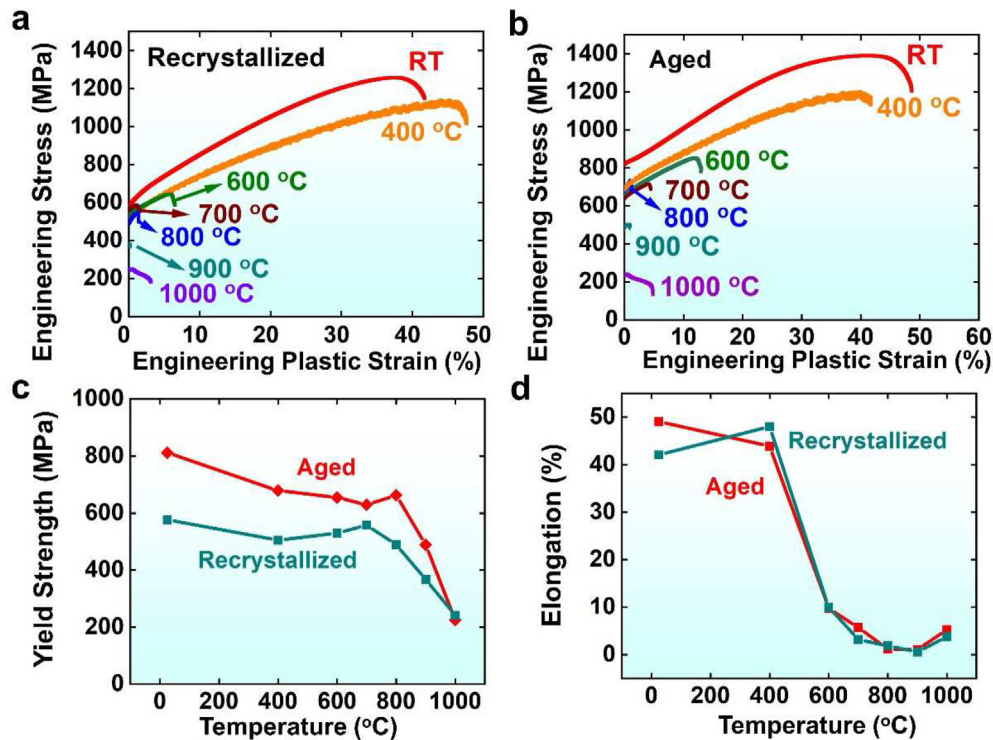
Fig. 7 − Mechanical properties of the recrystallized and aged Co002 alloys. Engineering stress-strain curves of (a) the recrystallized and (b) aged samples at temperatures ranging from RT to 1000 °C. (c) 0.2% offset yield strength, and (d) EF of the alloy as a function of temperature.

600 MPa when temperature below 800 °C. In addition, anomalous temperature dependence of yielding behavior also exists in both alloys, which is often reported in precipitation strengthened Ni-based superalloys [4,50−53]. As shown in Fig. 7c, when temperature increases, YS of these two alloys decrease slightly (from RT to 400 °C), remain unchanged or even increase slightly (600 °C−700 °C for recrystallized alloy, and 600 °C−800 °C for aged alloy), and then dramatically decrease. This anomalous yielding phenomenon at temperature ranging from 600 °C to 700/800 °C is similar to that found in γ′ precipitation strengthened Ni-based superalloys. It might be caused by the cross-slip of antiphase boundary (APB) from the {111} to {001} plane in γ′ phase [4,54]. Once the APB cross slips onto {001} plane, the super dislocation becomes sessile (so-called Kear-Wilsdorf lock), which can effectively resist deformation, thus the yield strength shows anomalous temperature dependence at this temperature region [4,54]. The temperature dependence of EF is shown in Fig. 7d. Clearly, temperature significantly affects the EF of alloys. When temperature is lower than 400 °C, EF is higher than 40%, indicating good ductility. However, when temperature exceeds 600 °C, EF dramatically decreases to lower than 10%, and reach the minimum at 800−900 °C (only ~ 2%). When temperature further increases to 1000 °C, EF increases to ~5%. The trend of EF with increasing temperature is similar with the so-called "intermediate temperature brittleness" in precipitation strengthened Ni-based superalloys [4,55,56].

Strength of the developed precipitation strengthened Co-based superalloy is promising. As shown in Fig. 8, at

temperatures ranging from RT to 1000 °C, strength of the Co002 alloy is much higher than that of traditional solid solution Co-based superalloys, such as widely used Haynes 188, Haynes 25 and MAR-M509 [10,57]. In addition, it is also
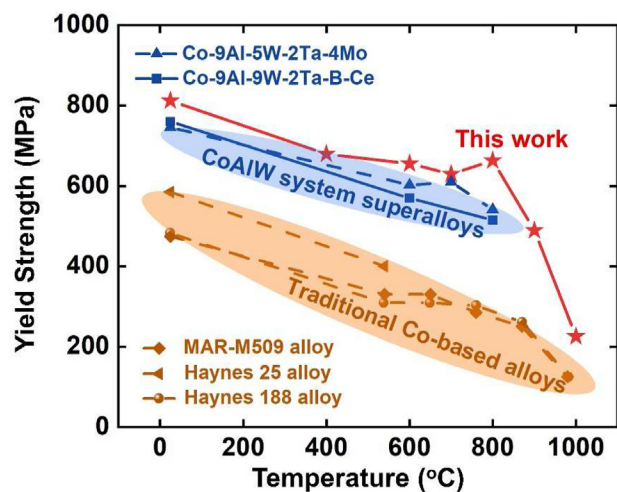
Fig. 8 − Temperature dependence of YS of the aged Co002, other traditional Co-based and Co−Al−W system alloys. Brown ellipse represents solid solution Co-based superalloys Haynes 188, Haynes 25 and MAR-M509 [10,57]). Blue ellipse represents Co−Al−W based precipitation strengthened superalloys [16,58].
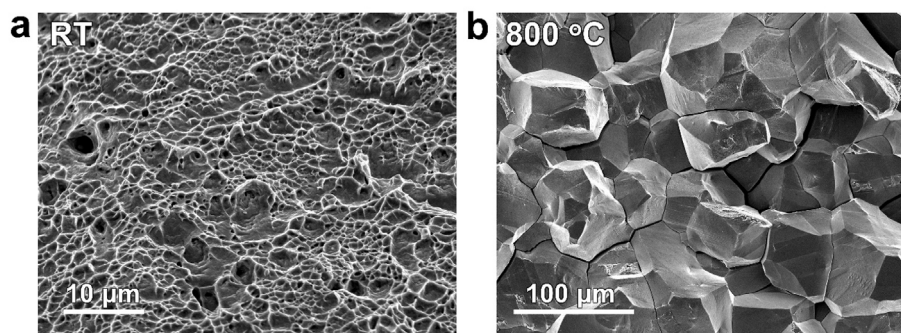
Fig. 9 − Fracture surfaces of the aged Co002 alloy after tensile tests at RT and 800 °C, respectively. (a) Dimple-like fracture surface indicates ductile fracture at RT. (b) Intergranular brittle fracture at 800 °C with the appearance of "rock candy".

comparable with or even slightly higher than that of precipitation strengthened Co−Al−W system superalloys, such as Co−9Al−9W−2Ta-0.02B-0.02Ce [58] and Co−9Al−5W−2Ta-0.02B−4Mo [16].

4.4. Deformation mechanism

To explore the deformation mechanism of the Co002 alloy after aging, fracture surfaces after tensile tests have been observed. At low temperatures (Fig. 9a), dimples are observed on the fracture surface, indicating ductile nature of the alloy. When temperature increases to higher than 600 °C, intergranular fracture occurs. For example, the fracture surface at 800 °C (Fig. 9b) consists of massive smooth facets and exhibits the appearance of "rock candy". Therefore, the intermediate

temperature brittleness of the γ' precipitation strengthened Co-based superalloys appears to originate from grain boundary brittleness, which is also commonly found in precipitation strengthened Ni-based superalloys [4,55].

Deformation behaviors of the aged Co002 alloy at different temperatures are investigated. As shown in Fig. 10a, the deformed microstructure are observed near the fracture surface. After fracture at low temperature (RT-400 °C), the original spherical γ' precipitates are stretched along tensile direction and become oval-shaped (Fig. 10b). In addition, massive shearing traces through both phases are observed, which are indicated by red arrows in Fig. 10b. When temperature increases to intermediate temperature (600−900 °C), there are still some shearing traces (red arrows in Fig. 10c) near the fracture, but the density of traces is much lower than
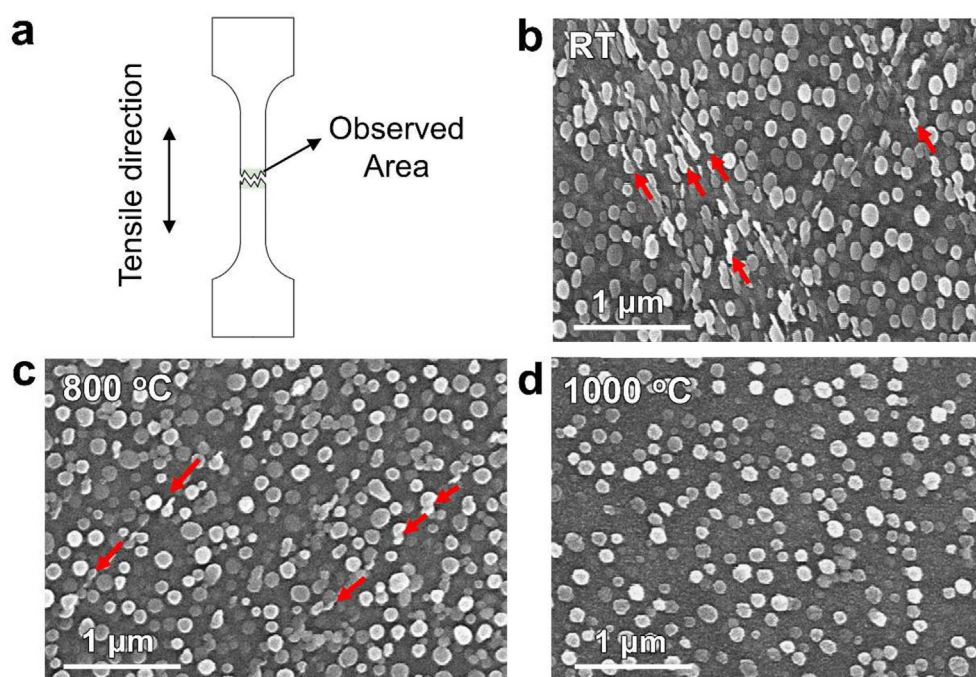

Fig. 10 − Microstructure of the aged Co002 alloy fractured at RT, 800 and 1000 °C. (a) Schematic illustration of the observed area for SEM characterization. (b−d) SE images showing deformed microstructures near the fracture surfaces after tensile testing at RT (b), 800 °C (c) and 1000 °C (d). The shearing traces are indicated by red arrows in (b) and (c).

that deformed at RT, which might be attributed to the reduced ductility at intermediate temperatures. However, at high temperature (1000 °C), there is no shearing trace anymore, and the γ′ precipitates are still spherical (Fig. 10d).

To reveal the deformation mechanism, TEM is used to characterize deformation substructure in the deformed alloy. Under ADF-STEM imaging mode, there are large amounts of bright strips in the grains of specimen fractured at RT,

indicated by arrows in Fig. 11a. The SADP shown as inset in Fig. 11a demonstrates that there are only diffraction spots of γ and γ′ phases without specific spots of twins or other phases, which reveals that those strips are slip bands. Figs. 11b & c are atomic-resolution HAADF-STEM images, indicating that defects in γ and γ′ phases are different. Defect in γ phase is an a/2<110> full dislocation, which dissociates into two a/6<112> partial dislocations and a stacking fault (SF) between them
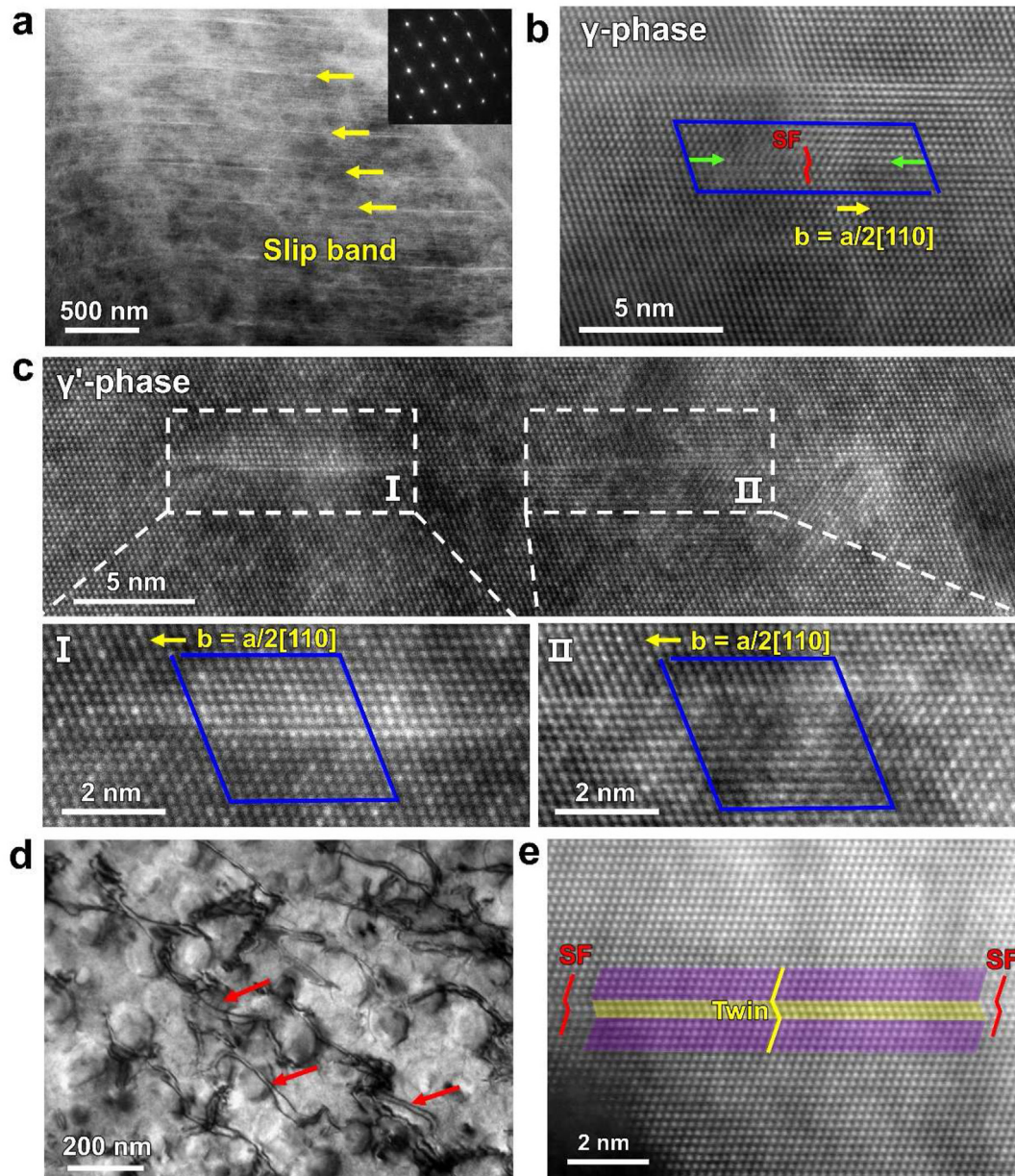
Fig. 11 − TEM/STEM characterization of the deformed specimens at RT. (a) STEM image of the fractured sample, indicating a large number of bright strips. SADP of these strips (shown as the inset), only with diffraction spots of γ and γ′ phases demonstrates that these strips are mainly dislocation slip bands (marked by the yellow arrows). (b, c) Atomic-resolution HAADF-STEM images showing defects in γ matrix (b) and γ′ phase (c). The defect in γ phase is an a/2 <110> full dislocation, which dissociates into two a/6<112> partial dislocations (paired green arrows) and a stacking fault (SF) between them, while the defect in γ′ phase is an a <110> superdislocation. The superdislocation consists of two a/2 <110> super partials (indicated by I and II in (c), respectively). (d) TEM image with about 10% plastic strain, indicating dislocation pairs (marked by red arrows) shearing the γ′ phase. (e) Atomic-resolution HAADF-STEM image showing a few short deformation twins (shorter than 12 nm) with thickness of three atomic layers.
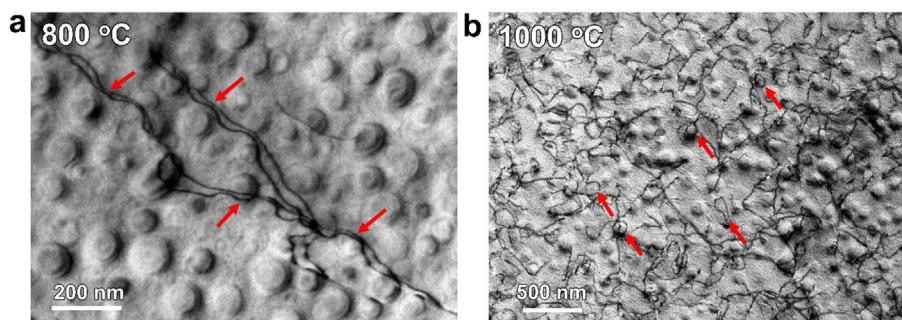
Fig. 12 — TEM characterization of the fractured specimens at 800 and 1000 °C, showing interaction between γ′ phase and dislocations in the deformed alloys. Dislocation pairs shearing γ′ phase are observed at 800 °C, while there are mainly tangled dislocations and dislocation loops surrounding γ′ phase at 1000 °C.

(Fig. 11b), which is commonly found in FCC solid solution alloys [59–61]. Defect in γ′ phase is an a <110> super dislocation consisting of two a/2<110> super partials, coupled by an APB between them (Fig. 11c). The two super partials are indicated by I and II in Fig. 11c, and their corresponding atomic resolution HAADF-STEM images are shown as insets in Fig. 11c. The two super partials have the same Burgers vector, which are both a/2[110]. However, high dislocation density in the fractured specimen obstructs observation of dislocation morphology, interrupted tensile test has been conducted at plastic strain about 10%. Fig. 11d shows that dislocation pairs consist of two a/2[110] dislocations (indicated by red arrows), which pass through both phases. These dislocation pairs are generally observed in deformed γ′ strengthened Ni-based superalloys [4,51]. Coordination of two a/2<110> dislocations in γ phase and a<110> super-dislocation in γ′ phase is responsible for the shearing of both phases (Fig. 10b).

Deformation twinning has been reported to be a dominant deformation mechanism for FCC CoNi-based alloys [60–63]. For examples, large amounts of deformation twins have been observed in CoNi-based solid solution alloys GH5188 (nominal composition is $Co_{40}Ni_{24}Cr_{27}Fe_4W_5$) and CoNiCr medium entropy alloy (MEA). However, as shown in SADP (inset of Fig. 11a), there is no deformation twins in the Co002 alloy fractured at RT. The volume fraction of twins might be too little to be distinguished in SADP, therefore atomic resolution TEM characterization has been carefully carried out. As shown in Fig. 11e, only a few three-layers nano-twins, whose length is shorter than 12 nm, have been observed. Generally, the lower the stacking fault energy (SFE, γ_{sf}), the easier the formation of deformation twins [64].

To determine the SFE, and compare with other alloys, more than ten 60° dislocations in the matrix of the Co002 alloy have been captured. Averaged width of dislocation cores in γ phase is determined to be 8.7 nm. Moreover, elastic constants, including ν and G, are needed. A FCC single phase alloy, whose composition is the same as the matrix of Co002 alloy, is prepared (details are shown in Supplementary Information). The ν and G of this alloy is determined to be 0.24 and 94 GPa, which should be the same as that of the matrix of the Co002 alloy. According to Eq. (3-1)Eq. (3-1), the SFE of the matrix is estimated to be only about 25 mJ/m². Therefore, the SFE of the matrix is similar with the CrCoNi MEA [61,63], where large

amounts of deformation twins have been observed after deformation at RT. The difficulty to form deformation twins in Co002 alloy might be attributed to the hindrance of partial dislocations by high density of γ′ precipitates [65–67]. Similar phenomenon has also been found in a Co—Al—Nb—Ni—Ti—Ta alloy [67], where the stacking faults are confined in the matrix, and the extension of the stacking faults are hindered by γ′ precipitates.

When temperature increases to intermediate temperature, the specimen fractures shortly after yield with plastic strain of only about 2% (Fig. 7b). It is clear that the fracture mode is intergranular fracture (Fig. 9b), indicating that grain boundary is weak at intermediate temperature. Consistent with the little plasticity, the dislocation density in the specimen fractured at 800 °C is extremely low (Fig. 12a). But a few dislocation pairs, which are passing through both phases, have still been found in TEM (red arrows in Fig. 12a), indicating that the deformation mode of Co002 alloy at intermediate temperature is similar to that at RT. However, when temperature increases to 1000 °C, the deformation mode is completely different. Large amounts of tangled dislocations (Fig. 12b) and dislocation loops surrounding the γ′ phase (indicated by red arrows) have been observed. These loops are probably dislocation debris after dislocations bypassing the γ′ phase, which are so-called Orowan loops [68,69]. Moreover, shearing trace has not been found and the shape of γ′ phase appears to be not changed after fracture at 1000 °C (Fig. 10d). Thus, plastic strain at 1000 °C is mainly caused by deformation of the γ matrix and γ′ precipitates serve as obstacles for dislocation motion, which provide high temperature strength. The deformation mechanism from RT to 1000 °C is consistent with other precipitation strengthened Co-based alloys, such as Co—Al—W alloy [70], Co—Ni—Al—W—Ti alloy [71].

5. Conclusion

A L1₂-structured γ′ precipitation strengthened Co-based superalloy is successfully fabricated and developed with the aid of thermodynamic calculation and experimental validation. Thermodynamic parameters, microstructure, mechanical properties and behaviors are investigated to reveal their relationship, which might provide guidelines for application

and development of precipitation strengthened Co-based superalloys. The main conclusions can be drawn as following:

1. A L1$_2$-structured γ′ precipitation strengthened Co-based superalloy is successfully fabricated with composition of Co9Al5Mo30Ni2Ta10CrB, whose matrix is FCC structure.
2. The spherical γ′ precipitates, which are coherent with the FCC matrix, are mainly formed during aging treatment (950 °C/4 h). The size and area fraction of the γ′ phase are about 100 nm and 55%, respectively.
3. The γ′ precipitation strengthened Co-based superalloy exhibits promising strength at a temperature range from RT to 1000 °C, which is much higher than that of traditional solid solution Co-based superalloys and comparable with or even slightly higher than precipitation strengthened Co−Al−W superalloys.
4. TEM characterization reveals that deformation is mainly dominated by shearing of both phases at temperatures from RT to 800 °C. When temperature further increases to 1000 °C, plastic strain is mainly caused by deformation of the matrix.

Credit authorship contribution statement

Zhouqing Zhang: Formal analysis, Investigation, Writing − original draft, Writing − review & editing. **Qingqing Ding**: Conceptualization, Methodology, Formal analysis, Investigation, Resources, Writing − original draft, Writing − review & editing. **Yilun Gong**: Formal analysis, Investigation, Writing − review & editing. **Xiao Wei**: Resources, Writing − review & editing. **Ze Zhang**: Conceptualization, Formal analysis, Resources, Writing − review & editing, Supervision. **Hongbin Bei**: Conceptualization, Methodology, Formal analysis, Investigation, Resources, Writing − original draft, Writing − review & editing, Supervision.

Data availability

Data will be made available on request.

Declaration of competing interest

The authors declare that they have no known competing financial interests or personal relationships that could have appeared to influence the work reported in this paper.

The raw/processed data required to reproduce these findings can be made available upon reasonable request to corresponding authors.

Acknowledgement

Appendix A. Supplementary data

Supplementary data to this article can be found online at https://doi.org/10.1016/j.jmrt.2023.09.154.

REFERENCES

[1] Kear ER, Thompson. Aircraft gas turbine materials and processes. Science 1980;208:847−56.
[2] Pollock TM, Tin S. Nickel-based superalloys for advanced turbine engines: chemistry, microstructure and properties. J Propul Power 2006;22:361−74.
[3] Suzuki A, Inui H, Pollock TM. Annu. Rev, L1$_2$-strengthened cobalt-base superalloys. Mater Res 2015;45:345−68.
[4] Reed RC. The superalloys fundamentals and applications. Cambridge: Cambridge University Press; 2006.
[5] Tzvetkoff T, Girginov A, Bojinov M. Corrosion of nickel, iron, cobalt and their alloys in molten salt electrolytes. J Mater Sci 1995;30:5561−75.
[6] Douglass DL, Bhide VS, Vineberg E. The corrosion of some superalloys in contact with coal chars in coal gasifier atmospheres. Oxid Met 1981;16:29.
[7] Misra AK. Corrosion of metals and alloys in sulfate melts at 750 °C. Oxid Met 1986;25:373.
[8] Pollock TM. Alloy design for aircraft engines. Nat Mater 2016;15:809−15.
[9] Jiang WH, Yao XD, Guan HR, Hu ZQ. Secondary M6C precipitation in a Cobalt-base superalloy. J Mater Sci 1999;34:2859.
[10] Coutsouradis D, Davin A, Lamberigts M. Cobalt-based superalloys for applications in gas turbines. Mater Sci Eng 1987;88:11−9.
[11] Sato J, Omori T, Oikawa K, Ohnuma I, Kainuma R, Ishida K. Cobalt-base high-temperature alloys. Science 2006;312:90−1.
[12] Omori T, Sutou Y, Oikawa K, Kainuma R, Ishida K. Shape memory and magnetic properties of Co-Al ferromagnetic shape memory alloys. Mater Sci Eng, A 2006;438:1045−9.
[13] Reed RC, Tao T, Warnken N. Alloy-by-design: application to nickel-based single crystal superalloys. Acta Mater 2009;57:5898−913.
[14] Warlimont H, Martienssen W. Springer handbook of materials data. Springer International Publishing; 2018.
[15] Feng G, Li H, Li SS, Sha JB. Effects of Mo additions on microstructure and tensile behaviors of a Co-Al-W-Ta-B alloy at room temperature. Scripta Mater 2012;67:499−502.
[16] Zhong F, Li S, Sha J. Tensile behaviour of Co-Al-W-Ta-B-Mo alloys with a coherent γ/γ′ microstructure at room and high temperatures. Mater Sci Eng, A 2015;637:175−82.
[17] Liu J, Yu JJ, Yang YH, Zhou YZ, Sun XF. Effects of Mo on the evolution of microstructures and mechanical properties in Co-Al-W base superalloys. Mater Sci Eng, A 2019;745:404−10.
[18] Freund LP, Stark A, Pyczak F, Schell N, Göken M, Neumeier S. The grain boundary pinning effect of the μ phase in an advanced polycrystalline γ/γ′ Co-base superalloy. J Alloys Compd 2018;753:333−42.
[19] Xue F, Li ZQ, Feng Q, Mo. Effect on the microstructure in Co-Al-W-based superalloys. Mater Sci Forum 2010;654−656:420−3.
[20] Makineni SK, Samanta A, Rojhirunsakool T, Alam T, Nithin B, Singh AK, et al. A new class of high strength high temperature Cobalt based γ-γ′ Co-Mo-Al alloys stabilized with Ta addition. Acta Mater 2015;97:29−40.
[21] Knop M, Mulvey P, Ismail F, Radecka A, Rahman KM, Lindley TC, et al. A new polycrystalline Co-Ni superalloy. JOM 2014;66:2495−501.

[22] Makineni SK, Nithin B, Chattopadhyay K. A new tungsten-free γ-γ´ Co-Al-Mo-Nb-based superalloy. Scripta Mater 2015;98:36–9.

[23] Klein L, Bauer A, Neumeier S, Göken M, Virtanen S. High temperature oxidation of γ/γ´-strengthened Co-base superalloys. Corrosion Sci 2011;53:2027–34.

[24] Neumeier S, Freund LP, Göken M. Novel wrought γ/γ´ cobalt base superalloys with high strength and improved oxidation resistance. Scripta Mater 2015;109:104–7.

[25] Chung DW, Toinin JP, Lass EA, Seidman DN, Dunand DC. Effects of Cr on the properties of multicomponent cobalt-based superalloys with ultra high γ´ volume fraction. J Alloys Compd 2020;832:154790.

[26] Sheykhlari AF, Arabi H, Boutorabi SMA, Cayron C. Effect of chromium content on microstructural evolution of CoNiAlW superalloy. Appl Phys A 2022;128:719.

[27] Ng DS, Chung DW, Toinin JP, Seidman DN, Dunand DC, Lass EA. Effect of Cr additions on a γ-γ´ microstructure and creep behavior of a Co-based superalloy with low W content. Mater Sci Eng, A 2020;778:139108.

[28] Yan HY, Vorontsov VA, Dye D. Alloying effects in polycrystalline γ´ strengthened Co-Al-W base alloys. Intermetallics 2014;48:44–53.

[29] Baler N, Pandey P, Singh MP, Makineni SK, Chattopadhyay K. Effects of Ti and Cr additions in a Co-Ni-Al-Mo-Nb-based superalloy. In: Superalloys 2020: proceedings of the 14th international symposium on superalloys; 2020. p. 929–36.

[30] Makineni SK, Singh MP, Chattopadhyay K. Low-density, high-temperature Co base superalloys. Annu Rev Mater 2021;51:187–208.

[31] Chen Y, Wang C, Ruan J, Omori T, Kainuma R, Ishida K, et al. High-strength Co-Al-V-base superalloys strengthened by γ´-Co₃(Al,V) with high solvus temperature. Acta Mater 2019;170:62–74.

[32] Chen Y, Wang C, Ruan J, Yang S, Omori T, Kainuma R, et al. Development of low-density γ/γ´ Co-Al-Ta-based superalloys with high solvus temperature. Acta Mater 2020;188:652–64.

[33] Wang H, Yang J, Meng J, Ci S, Yang Y, Sheng N, et al. Effects of B content on microstructure and high-temperature stress rupture properties of a high chromium polycrystalline nickel-based superalloy. JAC (J Antimicrob Chemother) 2021;860:157929.

[34] Jin K, Gao YF, Bei H. Intrinsic properties and strengthening mechanism of monocrystalline Ni-containing ternary concentrated solid solutions. Mater Sci Eng, A 2017;695:74–9.

[35] Ding Q, Li YK, Ouyang J, Zhang Z, Gao YF, Bei H, et al. The effect of stacking fault energy on the formation of nano twin/HCP during deformation in FCC concentrated solid solution (CSS) alloys. Mater Today Nano 2023;24:100407.

[36] Xu XD, Liu P, Tang Z, Hirata A, Song SX, Liu CT, et al. Transmission electron microscopy characterization of dislocation structure in a face-centered cubic high-entropy alloy Al0.1CoCrFeNi. Acta Mater 2018;144:107–15.

[37] Liu SF, Wu Y, Wang HT, He JY, Liu JB, Chen CX, et al. Stacking fault energy of face-centered-cubic high entropy alloys. Intermetallics 2018;93:269–73.

[38] Laplanche G, Kostka A, Reinhart C, Hunfeld J, Eggeler G, George EP. Reasons for the superior mechanical properties of medium-entropy CrCoNi compared to high-entropy CrMnFeCoNi. Acta Mater 2017;128:292–303.

[39] Fei X, Tao M, Meiling W, Xianfei D, Xianghui L, Qiang F. Effects of Ni on microstructural evolution and γ´ dissolution of novel Co-Al-W base alloys. Acta Metall Sin 2014;50:845–53.

[40] Kearsey RM, Beddoes JC, Jones P, Au P. Compositional design considerations for microsegregation in single crystal superalloy systems. Intermetallics 2004;12:903–10.

[41] Dahlen M, Winberg L. The influence of γ´-precipitation on the recrystallization of a nickel base superalloy. Acta Metall 1980;28:41–5.

[42] Ross EW, Sims CT. Superalloys II. New York: A Wiley-Interscience Publication; 1987. p. 97–133.

[43] Muller DA, Shashkov DA, Benedek R, Yang LH, Silcox J, Seidman DN. Atomic-scale studies of the electronic structure of ceramic/metal interfaces: {222} MgO/Cu. Mater Sci Forum 1999;294–296:99–102.

[44] Shashkov A, Chisholm MF, Seidman DN. Atomic-scale structure and chemistry of ceramic/metal interfaces - I. atomic structure of {222} MgO/Cu (Ag) interfaces. Acta Mater 1999;47:3939–51.

[45] Muller DA, Shashkov DA, Benedek R, Yang LH, Silcox J, Seidman DN. Atomic scale observations of metal-induced gap states at {222} MgO/Cu interfaces. Phys Rev Lett 1998;80:4721–44.

[46] Ross EW, Sims CT. Superalloys II. New York: A Wiley-Interscience Publication; 1987. p. 97–133.

[47] Nithin B, Samanta A, Makineni SK, Alam T, Pandey P, Singh AK, et al. Effect of Cr addition on γ–γ´ cobalt-based Co-Mo-Al-Ta class of superalloys: a combined experimental and computational study. J Mater Sci Technol 2017;52:11036–47.

[48] Yao X, Ding Q, Wei X, Wang J, Zhang Z, Bei H. The effects of key elements Re and Ru on the phase morphologies and microstructure in Ni-based single crystal superalloys. J Alloys Compd 2022:926.

[49] Shinagawa K, Omori T, Sato J, Oilawa K, Ohnuma I, Ishida K, et al. Phase equilibria and microstructure on γ´ phase in Co-Ni-Al-W system. Mater Trans 2008;49:1474–9.

[50] Hrutkay K, Kaoumi D. Tensile deformation behavior of a nickel based superalloy at different temperatures. Mater Sci Eng, A 2014;599:196–203.

[51] Ding Q, Bei H, Yao X, Zhao X, Wei X, Wang J, et al. Temperature effects on deformation substructures and mechanisms of a Ni-based single crystal superalloy. Appl Mater Today 2021;23:101061.

[52] Kozar RW, Suzuki A, Milligan WW, Schirra JJ, Sacage MF, Pollock TM. Strengthening mechanisms in polycrystalline multimodal nickel-base superalloys. Metall Mater Trans A 2009;40:1588–603.

[53] Ding Q, Bei H, Zhao X, Gao Y, Zhang Z. Processing, microstructures and mechanical properties of a Ni-based single crystal superalloy. Crystals 2020;10:572–85.

[54] Nabarro FRN, De Viliers HL. The physics of creep. Taylor & Francis; 1995. p. 109–18.

[55] Zhou Q, Ding Q, Zhang Y, Wei X, Zhang Z, Bei H. The application of in situ TEM on the grain boundary brittleness of precipitation-strengthened Ni-based superalloys: recent progress and perspective. Front Met Alloy 2022;1:1016638.

[56] Duan P, Zhang P, Li J, Li B, Gong XF, Yang GX, et al. Intermediate temperature brittleness in a directionally solidified nickel-based superalloy M4706. Mater Sci Eng, A 2019;759:530–6.

[57] Pike LM. 100+ years of wrought alloy development at haynes international. 8th International Symposium on Superalloy 718 and Derivatives; 2014. p. 15–30.

[58] Zhang BS, Yu YX, Tao ZL, Sha JB. A comparative study on microstructures and tensile behaviors of a novel polycrystalline and single-crystal Co-9Al-9W-2Ta-0.02B-0.02Ce alloy at room and high temperatures. Intermetallics 2021;137:107284.

[59] Ding Q, Bei H, Wei X, Gao YF, Zhang Z. Nano-twin-induced exceptionally superior cryogenic mechanical properties of a Ni-based GH3536 (Hastelloy X) superalloy. Mater Today Nano 2021;14:100110.

[60] Ding Q, Ouyang J, Zhang Y, Wei X, Zhang Z, Bei H. The universality of strength and plastic deformation in FCC concentrated solid solution (CSS) alloys at room and cryogenic temperatures. Appl Phys Lett 2022;21:121.

[61] George EP, Curtin WA, Tasan CC. High entropy alloys: a focused review of mechanical properties and deformation mechanisms. Acta Mater 2020;188:435—74.

[62] Xu XD, Liu P, Tang Z, Hirata A, Song SX, Liu CT, et al. Transmission electron microscopy characterization of dislocation structure in a face-centered cubic high-entropy alloy Al0.1CoCrFeNi. Acta Mater 2018;144:107—15.

[63] Gludovatz B, Hohenwarter A, Thurston KV, Bei H, Wu Z, George EP, et al. Exceptional damage-tolerance of a medium-entropy alloy CrCoNi at cryogenic temperatures. Nat Commun 2016;7:10602.

[64] Tian C, Han G, Cui C, Sun X. Effects of Co content on tensile properties and deformation behaviors of Ni-based disk superalloys at different temperatures. Mater Des 2015;88:123—31.

[65] Pandey P, Heczko M, Khatavkar N, Mazumder N, Sharma A, Singh A. On the faulting and twinning mediated strengthening and plasticity in a γ' strengthened CoNi-based superalloy at room temperature. Acta Mater 2023:252.

[66] Zhao Y, Zhang Y, Luo Y, Tang D, Liu H, Fu H. Deformation behavior and creep properties of Co-Al-W-based superalloys: a review. Prog Nat Sci-Mater 2021;31:641—8.

[67] Cao BX, Xu WW, Yu CY, Wu SW, Kong HJ, Liu CT, et al. L1$_2$-strengthened multicomponent Co-Al-Nb-based alloys with high strength and matrix-confined stacking-fault-mediated plasticity. Acta Mater 2022;229.

[68] Gleiter H, Hornbogen E. Precipitation hardening by coherent particles. Mater Sci Eng, A 1968;2:285—302.

[69] Blum W, Reppich B. Creep of particle-strengthened alloys. In: Wilshire B, Evans RW, editors. Creep behaviour of crystalline solids. Swansea: Pineridge Press; 1985. p. 83—135.

[70] Suzuki A. High-temperature strength and deformation of γ/γ' two-phase Co-Al-W-base alloys. Acta Mater 2008;56:1288—97.

[71] Shi L, Yu JJ, Cui CY, Sun XF. Microstructural stability and tensile properties of a Ti-containing single-crystal Co-Ni-Al-W-base alloy. Mater Sci Eng, A 2015;646:45—51.